CHARGE CONSERVATION IN ELECTROMAGNETIC PIC CODES; SPECTRAL COMPARISON OF BORIS AND MARDER METHODS

by

P. J. Mardahl and J. P. Verboncoeur

Memorandum No. UCB/ERL M96/83

20 December 1996

CHARGE CONSERVATION IN ELECTROMAGNETIC PIC CODES; SPECTRAL COMPARISON OF BORIS AND MARDER METHODS

by

P. J. Mardahl and J. P. Verboncoeur

Memorandum No. UCB/ERL M96/83

20 December 1996

ELECTRONICS RESEARCH LABORATORY

College of Engineering
University of California, Berkeley
94720

Charge conservation in electromagnetic PIC codes; spectral comparison of Boris and Marder methods

P. J. Mardahl and J. P. Verboncoeur
Department of Electrical Engineering and Computer Science
University of California, Berkeley
Berkeley, CA 94720-1770
peterm@langmuir.eecs.berkeley.edu

Abstract

Non-charge conserving current collection algorithms for electromagnetic PIC plasma simulations may cause errors in Gauss's law. These errors arise from violations of the charge continuity equation, $\nabla \cdot \mathbf{J} = -\partial\rho/\partial t$, which in turn cause errors in the irrotational part of $\mathbf{E}$.

Two techniques for reducing these errors are examined and compared: a modified Marder correction which corrects electric fields locally and primarily affects short wavelengths, and a Boris divergence correction, which solves Poisson's equation to correct the electric fields so that Gauss's law is enforced globally. The effect of each method on the spectrum of the error is examined. Computational efficiency and accuracy of the two techniques are compared: neither method is clearly superior.

Cases examined include corrections in electromagnetic relativistic beam simulations, and a hot thermal plasma. In addition, the spectral comparison provides insight into the behavior of the schemes applied.

1 Introduction

In electromagnetic particle-in-cell (PIC) simulations, a number of approximations have to be made in order to model the physics on a digital computer in a reasonable time. These approximations introduce errors in the simulation which could affect the physics.

The particular approximations which are commonly made include: discretizing space for the purposes of solution of Maxwell's curl equations ($\nabla \times \mathbf{H} = \mathbf{J} + \partial\mathbf{D}/\partial t$, $\nabla \times \mathbf{E} = -\partial\mathbf{B}/\partial t$) on a mathematical mesh; the use of many fewer particles than would exist in a real system, although the charge to mass ratio is the same; weighting of current to the mathematical mesh from these discrete particles in order to form the source term $\mathbf{J}$ for solving the curl equations; and the weighting of the fields from the mathematical mesh to the particles to calculate their motion. These approximations are typical of classical PIC models, such as in [1] and [2].

All of these approximations lead to error: the goal is to keep the error small enough so that the simulation is modeling the desired physics appropriately. The focus of this work is to study the accumulation of errors resulting from mapping the current of discrete charged particles onto a numerical mesh, and methods of reducing these errors. The errors arise when the current and charge density mapped to the mesh violate the continuity equation. A number of authors have noted this problem [1, 3, 4].

Non-charge conserving current weightings, such as a linear current weighting used in combination with a linear charge weighting, violate the continuity equation, $\nabla \cdot \mathbf{J} = -\partial\rho/\partial t$, in turn causing errors in Gauss's law, $\nabla \cdot \mathbf{D} = \rho$. However, these linear current weightings reduce noise in comparison with the charge conserving method described by Villasenor and Buneman [5]. When noise is an issue, one may choose to use the higher order weighting in conjunction with a correction scheme in order to reduce the violation of Gauss's law. However, higher order weightings are more computationally intensive and complicate boundary conditions.

Presented here are some methods which can be used to reduce cumulative errors in Gauss's law due to slightly non-charge-conserving current weightings from the particles to the mesh, and the results observed when these methods are applied to a variety of problems.

Section 1.1 defines the corrections used, and Section 1.2 describes the simulation and analysis methods. Section 2.1 gives results for removal of a delta function source test case, Section 2.2 for single-wavelength errors. In Sections 2.3 and 2.4 results for relativistic beams are presented. Section 2.5 shows results for a very hot thermal plasma. Conclusions are given in Section 3.

1.1 Corrections Used

1.1.1 Boris Correction

The Boris-type correction (modified slightly from [1]) is given by:

$$\mathbf{E}_{corrected} = \mathbf{E} - \nabla\delta\phi \tag{1}$$

such that

$$\nabla \cdot \epsilon \mathbf{E}_{corrected} = \rho \tag{2}$$

where $\mathbf{E}_{corrected}$ is an electric field which obeys Gauss's law, and $\nabla\delta\phi$ is the correction to $\mathbf{E}$, the uncorrected field. Combining Eqs. (1) and (2), we obtain:

$$\nabla \cdot (\epsilon \mathbf{E} - \epsilon \nabla \delta\phi) = \rho \tag{3}$$

so we require a solution for $\delta\phi$, with $\mathbf{E}$ and ρ given, to the elliptic equation:

$$\nabla \cdot \epsilon \nabla \delta\phi = \nabla \cdot \epsilon \mathbf{E} - \rho. \tag{4}$$

This elliptic equation can be solved using a number of direct and iterative schemes with varying degrees of efficiency.

1.1.2 Langdon-Marder Correction

The Marder-type scheme used is the one proposed by A.B. Langdon [3]. He proposed essentially the following scheme, which has been slightly modified to allow for inhomogeneous permittivity, ϵ:

$$\epsilon \mathbf{E}^{n+1}_{corrected} = \epsilon \mathbf{E}^{n+1} + \Delta t \nabla [d(\nabla \cdot \epsilon \mathbf{E}^{n+1} - \rho^{n+1})] \tag{5}$$

This is a modification of the Marder scheme, which is less implicit:

$$\epsilon \mathbf{E}^{n+1}_{corrected} = \epsilon \mathbf{E}^{n+1} + \Delta t \nabla [d(\nabla \cdot \epsilon \mathbf{E}^{n} - \rho^{n})] \tag{6}$$

where d is the diffusion parameter, which should satisfy (in two dimensions):

$$d \leq \frac{1}{2\Delta t}\left(\frac{\Delta x^2 \Delta y^2}{\Delta x^2 + \Delta y^2}\right) \equiv d_{max} \tag{7}$$

to ensure stability of the method [3]. The superscripts n, $n+1$ indicate simulation timestep: Langdon's proposed modification is simply to use the $\mathbf{E}$ and ρ at the current time rather than from the previous timestep.

1.1.3 Irrotationality of the correction

Both the Boris and the Langdon-Marder corrections arise from the gradient of a scalar field, $\nabla\delta\phi$, which can be seen from Equations (4) and (5). This, combined with the vector identity $\nabla \times \nabla\delta\phi \equiv 0$, demonstrates that both corrections have no effect on the solenoidal part of the field. This property is important, since only the solenoidal part of the electric field is used in advancing the magnetic field in time via $\nabla \times \mathbf{E} = -\partial\mathbf{B}/\partial t$; hence both methods only operate on the irrotational part of $\mathbf{E}$.

1.2 Models and Implementation

The methods were implemented and tested within the framework of the XOOPIC two-dimensional electromagnetic PIC code [6]. For this study, standard PIC methods [1] were used for advancing particles and fields. In the interest of clarity and convenience of Fourier analysis, this investigation is performed on a uniform Cartesian mesh. The testing space was discretized into either a 16x16, 32x32, or 64x64 square mesh bounded by conductors.

Figure 1 illustrates the locations of the field components on the mesh (which is a standard Yee mesh [7]). Electric field **E** and current **I** are defined at the midpoints of lines connecting the nodes of the mesh, while ρ and ϕ are defined on the nodes.

The Boris correction was implemented by using the Dynamic Alternating Direction Implicit (DADI) [8] method to solve Eq. (4), which is discretized using the standard 5-point stencil for ϕ:

$$\frac{\phi_{i-1,j} - 2\phi_{i,j} + \phi_{i+1,j}}{\Delta x^2} + \frac{\phi_{i,j-1} - 2\phi_{i,j} + \phi_{i,j+1}}{\Delta y^2} \tag{8}$$

The DADI method is an iterative scheme which makes use of a "fictitious timestep" to attempt to speed up convergence to a correct solution. Successive iterations of DADI will choose successive "fictitious timesteps" using a heuristic rule. If a poor choice of initial "fictitious timestep" is made, the problem will take longer to converge to the solution.

The Langdon-Marder correction was implemented by casting Eq. (5) into finite difference form as in the following example for one component of **E**:

$$\epsilon \mathbf{E}^{n+1}_{x,j+1/2,k\ corrected} = \epsilon \mathbf{E}^{n+1}_{x,j+1/2,k} + \frac{\Delta t}{\Delta x}(d_{j+1,k} Err^{n+1}_{j+1,k} - d_{j,k} Err^{n+1}_{j,k}) \tag{9}$$

where Err is the divergence error, calculated by:

$$Err_{j,k} = \Delta y(\epsilon \mathbf{E}_{y,j,k+1/2} - \epsilon \mathbf{E}_{y,j,k-1/2}) + \Delta x(\epsilon \mathbf{E}_{y,j,k+1/2} - \epsilon \mathbf{E}_{y,j,k-1/2}) - \rho_{j,k} \tag{10}$$

The wavelength components of the error are analyzed using a one dimensional Fast Fourier Transform along each mesh-line, producing k_x vs. y, and k_y vs. x. Only a finite set of wavelengths are observable: those for which $0 \leq k_x \Delta x \leq \pi$.

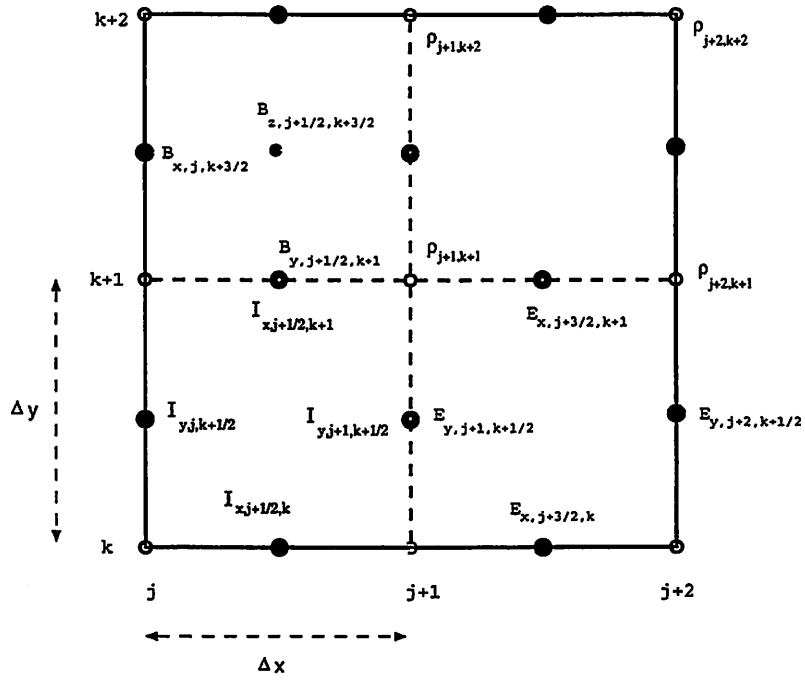

Figure 1: Yee mesh for current and electric field.

2 Results

2.1 Delta Function Source Test Case

The methods were tested first on a delta function source, by setting $\mathbf{E}^{t=0}(x,y) = 0$ and setting $\rho = \delta(x - x_0)\delta(y - y_0)$. A delta function has the property of having components at every wavelength. This allows examination of the behavior of each correction on all wavelengths simultaneously.

For this case, the bounded, square system is loaded in the center with the closest approximation to a delta function source possible on a discrete mesh: a nonzero charge density at only one mesh point. The walls are grounded ideal conductors on which potentials satisfy a Dirichlet condition. All corrections should relax to the Poisson solution in the system for a line charge, or equivalently, reduce the error in Gauss's law to zero.

2.1.1 Boris Correction on the Delta Function Source

Applying the Boris correction to a delta function source shows the wavenumber dependence of the error as a function of iteration. The scales of Figure 2 are logarithmic over 9 orders of magnitude, so a noticeable drop in amplitude is actually fairly large.

The error $f(k)$ starts at a (normalized) value of 1 for all wavelengths. The DADI-based Boris correction requires a few iterations to "settle in", and find the correct internal parameter for the most rapid convergence to the proper solution. The parameter is a "fictitious timestep"; it is adjusted at each iteration by the DADI algorithm.

The first try at reducing the error shows that a non-optimal initial "fictitious timestep" was chosen. Little removal of the error occurred for the first five timesteps. After that, a rapid attenuation of short wavelength errors (k_x large) occurred.

At iteration 79, (Figure 2b), the error is reset to 1, and the "fictitious timestep" from the $78th$ iteration of previous problem is used to restart the iterations. In this case, it is the error at long wavelengths which are removed fastest at first, and some amount of short wavelength error remains even after 40 iterations. Evidently, the "fictitious timestep" restarted at such a value as to remove the long wavelengths most quickly. The initial convergence is somewhat better, although the error is not reduced as much after 40 iterations. In this example, changing the initial timestep improved the convergence in early iterations, but converged more slowly at the $40th$ iteration.

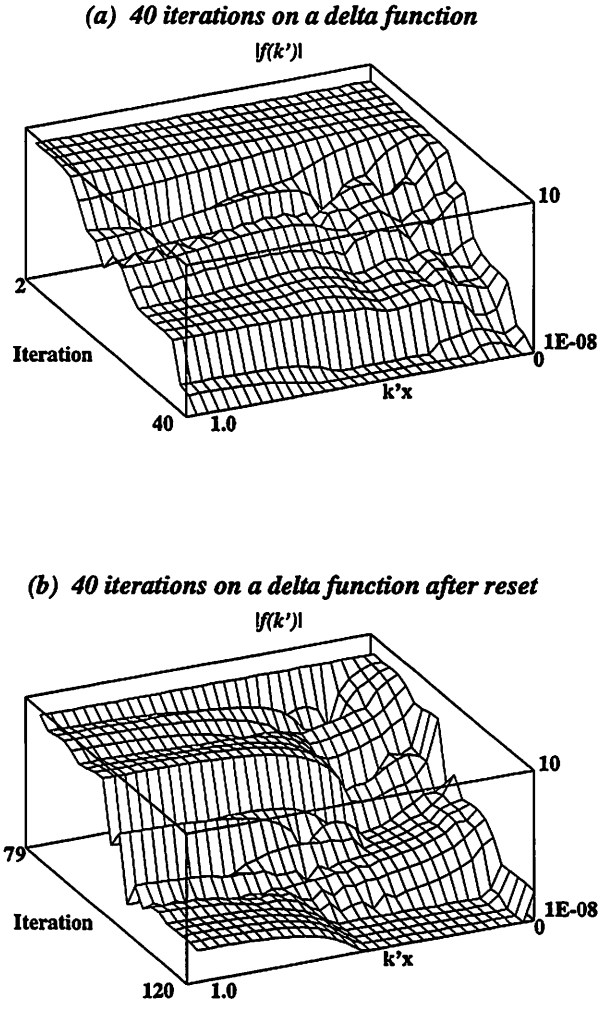

Figure 2: The effect of 40 iterations of DADI on the error $f(k)$. $k' \equiv k\Delta x/\pi$ is a normalized wavenumber. (a) uses a non-optimal choice of initial "fictitious timestep", which is improved in (b).

2.1.2 Langdon-Marder Correction on the Delta Function Source

Next, the Langdon-Marder correction is applied to the delta function source. Longer wavelengths are removed less quickly by the Langdon-Marder correction than the Boris correction (comparing Figs. 2 and 3), while shorter wavelengths are removed much more efficiently when the numerical parameter d is chosen to be close to the maximum value possible for stability of the algorithm.

Nevertheless, even with the choice of a large d, the overall magnitude of the error does not drop as quickly (compared to the DADI-based Boris correction) per iteration. This is balanced by the fact that each Langdon-Marder iteration is much less expensive than each DADI-based Boris iteration.

The Langdon-Marder correction monotonically reduces the error to zero (Langdon shows that the Langdon-

Marder correction is equivalent to point Jacobi iteration, which is known to converge [3]), while the DADI-based Boris correction does not converge monotonically.

The choice of diffusion parameter d also seems to influence the wavelength at which fastest convergence occurs. However, very long wavelength errors are still attenuated slowly: 150 iterations were needed in some cases to reduce the error at the longest wavelength by a factor of 2 with a diffusion parameter of $d = d_{max}$.

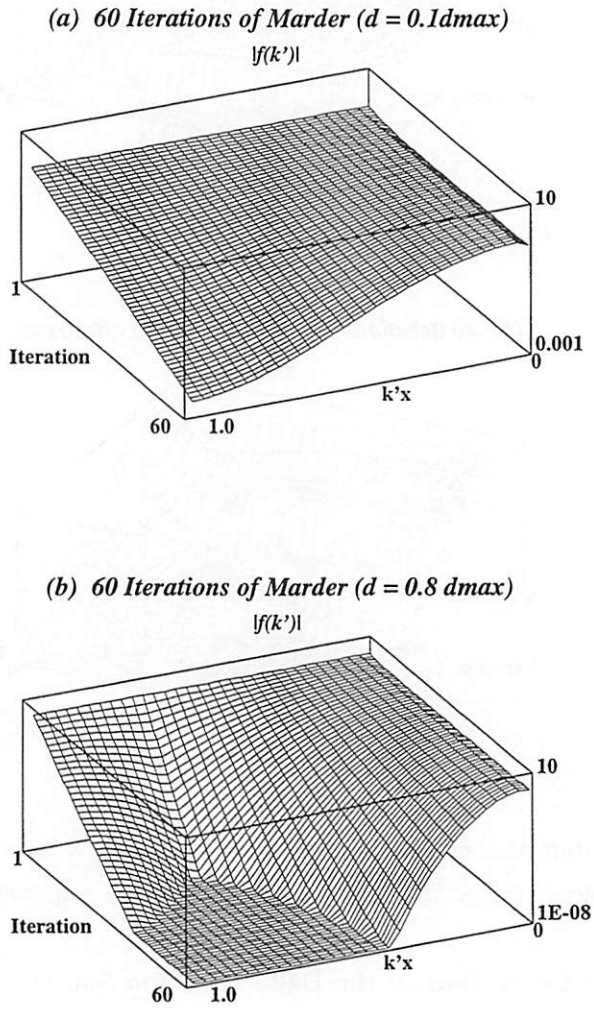

Figure 3: Attenuation of error as the Langdon-Marder correction is iterated. $k' \equiv k\Delta x/\pi$ is a normalized wave number. (a) was computed using $d = 0.1d_{max}$, where d_{max} is defined by (7). The flat part of the graph at 10^{-8} is an artifact of the graphing program; the actual value of the error there is smaller than 10^{-8}.

2.2 Single Wavelength Test Cases

It is also of interest to examine the spectral diffusivity properties of these methods. This can be done by adding a divergence error at a single wavenumber and observing the spectral purity after repeated applications of the method.

Accordingly, error test cases of the form

$$\nabla \cdot \mathbf{D} - \rho = sin(\frac{n\pi x}{L_x})sin(\frac{n\pi y}{L_y}) \tag{11}$$

were examined, where n is an integer and L_x, L_y are the dimensions of the system. This type of error shows up as discrete spikes in Fourier transforms, since only a single wavenumber is introduced. The values of n examined were chosen so that 1, 2, 4, 8, and 16 waves could be observed in the system.

For both the Langdon-Marder and Boris corrections, the spikes in k-space remained discrete and did not spread out. The error remained in one wavelength until the error was of the order of machine precision. Even errors with multiple wavelengths introduced at the outset had this property, although each wavelength of error was removed at a different rate. Since all observable wavelengths are present in Figs. 2 and 3, one can observe the convergence rates by wavelength.

2.3 Relativistic Beam Test Case

The delta function source test case and the single-wavelength source test cases were somewhat contrived, in that a divergence error was simply introduced into the system arbitrarily. Those sources were studied to provide insight into the spectral behavior of the different corrections.

It is also desirable to examine cases in which the error arises from sources natural to simulations: the actual errors introduced by moving simulated particles. In this case, a simulated beam with a very high velocity (0.967 c) was injected into the system along the x direction. The beam had a low current ($I = 1A$, with a crossection of 1 square meter) and a high energy such that the particles drift unperturbed through the system; i.e, $q\mathbf{E}\Delta t/m \ll \sqrt{2\mathcal{E}/m}$ where $\mathcal{E}$ is the initial beam energy and $\mathbf{E}$ is the electric field. These errors are different in character than the test-cases previously shown, as is evident from Figures 4 and 5.

This example is interesting because it can generate large errors every timestep for a current weighting which is non-charge conserving. The error is shown in Figure 4. Notable is the presence of long-wavelength components in the error, as is evident from Figure 5.

In Figure 6, we show the effect of applying the corrections. In this figure, two iterations of the DADI-based Boris correction enjoy comparable success to 10 iterations of the Langdon-Marder correction. However, in the top graph, the DADI method is much more successful in reducing the error in longer wavelengths but less successful in shorter wavelengths than the Langdon-Marder correction. In the bottom graph, both methods enjoy comparable success.

Figure 7 shows an overall figure of merit for the removal of the error. This figure was calculated as follows:

$$\sum_{cells} \left(\oint_{cell} \mathbf{D} \cdot d\mathbf{S} - Q_{cell}) \right) / \sum_{cells} Q_{cell} \tag{12}$$

The Langdon-Marder and DADI-based Boris correction performed comparably well. Two DADI iterations were used for the Boris correction, and 10 iterations using $d = 0.8 d_{max}$ for the Langdon-Marder correction.

2.4 Beam with a large perpendicular magnetic field applied

This case is similar to the previous case except a magnetic field (63 Gauss) was applied in the z direction to turn the beam, and a beam was injected from the left of the system as well as from the right. Both beams were one Ampere, and travelling with a velocity of 0.967c. Figure 8 shows only the rightward-moving beam. The two beams pass through each other with little perturbation, since $q\mathbf{E}\Delta t/m \ll \sqrt{2\mathcal{E}/m}$, where $\mathbf{E}$ is the electric field and $\mathcal{E}$ is the beam energy.

The error spectra observed in this case (not shown) were very similar to the spectra observed for the previous relativistic beam case, for the uncorrected simulation as well as for the Langdon-Marder and Boris corrected simulations. The corrections were applied in the same way as the previous example: 10 passes of Langdon-Marder correction with $d = 0.8d_{max}$, and 2 iterations of the DADI-based Boris correction. One notable difference is that there is a stronger DC ($k = 0$) component than in the previous case, which was shown in Fig. 5. The stronger DC component probably explains why the DADI correction performed a little better than the Langdon-Marder correction in Figure 9. As was demonstrated by Figure 3, the Langdon-Marder correction is not as efficient at removing long-wavelength errors.

2.5 Thermal Plasma

In this case a simulation of a very hot uniform plasma (T = 4700eV, $n_i = n_e = 10^{16}m^{-3}$) is examined. At this temperature the electron thermal speed is 3×10^7m/s. The plasma is uniform with very heavy (M/m = 40000) ions at T = 1.87eV.

Figure 10 shows the time dependence of the magnitude of the divergence error for the cases of (1) uncorrected, (2) Langdon-Marder-corrected, and (3) DADI/Boris corrected. The same number of iterations and diffusion parameter were used as in the previous cases: 10 Langdon-Marder iterations at $d = 0.8d_{max}$ and 2 iterations of DADI. The DADI-based Boris correction was again a little more successful at removing overall error in the system. Again, the error spectra is similar to that already given in Fig. 5.

3 Conclusions

Tests on single-wavelength errors showed that both methods of removing errors are non-dispersive, that is, an error at one wavelength will not spread to other wavelengths as the corrections are applied.

Divergence errors are not necessarily dominated by short wavelength errors for PIC simulations. Instead, errors were observed over a broad range of wavelengths. This broad spectrum reduces the efficacy of methods such as the Langdon-Marder method, which preferentially remove short wavelength errors.

The magnitude of the diffusion parameter d used by the Langdon-Marder-type correction also had some effect on the convergence rate for different wavelengths, although this effect was not very pronounced. Essentially, the k of fastest attenuation of error varied somewhat depending on the value of d: the closer d was chosen to d_{max}, the shorter the wavelength of fastest attenuation. However, even with d near d_{max}, attenuation of long wavelengths was slow.

The divergence error injected per timestep can be large when the particles are moving very quickly, and thus error can be introduced even more quickly than it can be removed by some corrections. In these cases, a non-charge conserving current algorithm may not be practical.

The divergence error was not observed to increase without bound, but rather reached a final value asymptotically, on the order of 1/100 to 1/1000.

The Boris correction based on the Dynamic ADI method proved to be as efficient at removing errors in the PIC simulations examined as the Langdon-Marder correction used. Five iterations of the Langdon-Marder correction is about as expensive computationally as one iteration of the DADI-based Boris correction as implemented in XOOPIC. Unfortunately, they both produce almost the same amount of correction overall, so one cannot choose the better method based on efficiency in error removal.

The Langdon-Marder correction is much more straighforward to implement than a Poisson solver, but a Poisson solver may already exist in the code for other purposes, e.g., an electrostatic field solver. The Langdon-Marder correction is clearly easier to adapt to parallel processing architectures due to the local nature of the algorithm. However, the Boris correction is simply a matrix inversion, amenable to library routines. Both methods will scale as the number of nodes in the mathematical mesh.

4 Acknowledgments

This work was performed partially with the support of the AFOSR/ASSERT Grant F49620-92-J-04876, and AFOSR/MURI Grant F49620-95-1-0253. Dr. Dennis Hewett of LLNL provided help with the DADI method. Thanks go to Prof. C.K. Birdsall and Dr. A. Bruce Langdon of LLNL for their consultation.

A How Errors in Gauss's Law Arise in PIC Simulations

To fit the discrete mathematical mesh, we recast $\nabla \cdot \mathbf{D} = \rho$ as $\oint_S \mathbf{D} \cdot dS = \int_V \rho dV$ around each grid node as shown in Figure 11.

A.1 One-dimensional non-conservation of charge

Consider this one dimensional example of how linear weighting of current and charge could lead to a violation of continuity, which in turn leads to a violation of Gauss's law. In this example, a particle of charge Q moves from position p_1 to p_2, in a single timestep of length Δt.

Assuming this is the only particle in motion, this would lead to the accumulation of the following charges at mesh points, using a linear weighting of the charge to adjacent mesh points:

$$q_1^t = \frac{x_2 - p_1}{x_2 - x_1} Q \tag{13}$$

$$q_2^t = \frac{p_1 - x_1}{x_2 - x_1} Q \tag{14}$$

$$q_1^{t+\Delta t} = \frac{x_2 - p_2}{x_2 - x_1} Q \tag{15}$$

$$q_2^{t+\Delta t} = \frac{p_2 - x_1}{x_2 - x_1} Q \tag{16}$$

$$\Delta q_1 = q_1^{t+\Delta t} - q_1^t = \frac{p_1 - p_2}{x_2 - x_1} Q \tag{17}$$

$$\Delta q_2 = q_2^{t+\Delta t} - q_2^t = \frac{p_2 - p_1}{x_2 - x_1} Q \tag{18}$$

where p_1, p_2 are initial and final particle positions, x_j are grid positions, Q is the charge of the particle moving, q_j are the charges weighted to the mesh, t is the time, and Δt is the time it took for the particle to move from p_1 to p_2.

Linear weighting of the current is done by first finding the midpoint of the displacement of the particle, and then using that midpoint to weight the current to the nodes (as in [1] pp. 358-364). Then, the current at the nodes is averaged to obtain the current at the half-nodes.

$$I_{midpoint} = \frac{Q(p_2 - p_1)}{\Delta t (x_2 - x_1)} \tag{19}$$

$$I_1 = \left(x_2 - \frac{p_2 + p_1}{2} \right) \frac{I_{midpoint}}{x_2 - x_1} \tag{20}$$

$$I_2 = \left(\frac{p_2 + p_1}{2} - x_1 \right) \frac{I_{midpoint}}{x_2 - x_1} \tag{21}$$

$$I_{\frac{1}{2}} = \frac{0 + I_1}{2} = \left(x_2 - \frac{p_2 + p_1}{2} \right) \frac{I_{midpoint}}{2(x_2 - x_1)} \tag{22}$$

$$I_{\frac{3}{2}} = \frac{I_2 + I_1}{2} = \frac{I_{midpoint}}{2} \tag{23}$$

$$I_{\frac{5}{2}} = \frac{I_2 + 0}{2} = \left(\frac{p_2 + p_1}{2} - x_1 \right) \frac{I_{midpoint}}{2(x_2 - x_1)} \tag{24}$$

We sum the currents into and out of each node to calculate the change in charge:

$$\Delta q_0 = -I_{\frac{1}{2}}\Delta t \tag{25}$$

$$\Delta q_1 = (I_{\frac{1}{2}} - I_{\frac{3}{2}})\Delta t \tag{26}$$

$$\Delta q_2 = (I_{\frac{3}{2}} - I_{\frac{5}{2}})\Delta t \tag{27}$$

$$\Delta q_3 = I_{\frac{5}{2}}\Delta t \tag{28}$$

After performing some algebra, we have:

$$\Delta q_0 = \left(\frac{p_2 + p_1}{2} - x_2\right)\frac{Q(p_2 - p_1)}{2(x_2 - x_1)^2} \tag{29}$$

$$\Delta q_1 = \left(x_1 - \frac{(p_1 + p_2)}{2}\right)\frac{Q(p_2 - p_1)}{2(x_2 - x_1)^2} \tag{30}$$

$$\Delta q_2 = \left(x_2 - \frac{(p_1 + p_2)}{2}\right)\frac{Q(p_2 - p_1)}{2(x_2 - x_1)^2} \tag{31}$$

$$\Delta q_3 = \left(\frac{p_2 + p_1}{2} - x_1\right)\frac{Q(p_2 - p_1)}{2(x_2 - x_1)^2} \tag{32}$$

Equations (30) and (31) disagree with Eqs. (17) and (18). Since the currents $I_{\frac{1}{2}}, I_{\frac{3}{2}}, I_{\frac{5}{2}}$ are the source currents used to advance Maxwell's curl equations, $\nabla \times \mathbf{H} = \mathbf{J} + \partial\mathbf{D}/\partial t$ and $\nabla \times \mathbf{E} = -\partial\mathbf{B}/\partial t$, the resultant electric fields reflect a different change in charge at the nodes, i.e., a violation of continuity leading to a violation of Gauss's law.

Similar difficulties arise with weighting currents directly to the half-cells as in Figure 13.

This weighting results in the following expressions:

$$I_{1/2} = \frac{I_{midpoint}}{x_1 - x_0}\left(\frac{x_1 + x_2}{2} - \frac{p_1 + p_2}{2}\right) \tag{33}$$

$$I_{3/2} = \frac{I_{midpoint}}{x_1 - x_0}\left(\frac{p_1 + p_2}{2} - \frac{x_1 + x_0}{2}\right) \tag{34}$$

$$\Delta q_0 = \frac{Q(p_2 - p_1)}{2(x_1 - x_0)^2}\left((x_1 + x_2) - (p_1 + p_2)\right) \tag{35}$$

$$\Delta q_1 = \frac{Q(p_2 - p_1)}{2(x_1 - x_0)^2}\left(\frac{x_0 + 2x_1 + x_2}{2} - (p1 + p2)\right) \tag{36}$$

$$\Delta q_2 = \frac{Q(p_2 - p_1)}{2(x_1 - x_0)^2}((p_1 + p_2) - (x_1 + x_0)) \tag{37}$$

which again differ from Equations (17) and (18).

However, not all current weightings will disagree with the linear weighting of charge to the grid. If one weights all the current to the nearest half grid point[1, 5], then the current will agree with Equations (17) and (18). The following equations show this: (refer to Figure 13 for definitions.)

$$I_{1/2} = 0 \tag{38}$$

$$I_{3/2} = \frac{Q(p_2 - p_1)}{\Delta t(x_2 - x_1)} \tag{39}$$

$$\Delta q_1 = -I_{3/2}\Delta t = \frac{p_1 - p_2}{x_2 - x_1}Q \tag{40}$$

$$\Delta q_2 = I_{3/2}\Delta t = \frac{p_2 - p_1}{x_2 - x_1}Q \tag{41}$$

Figure 14 illustrates the distribution of charge to the grid for the different current weightings. The figure shows the integrated net charge at a node due to current weighted from a particle of constant velocity. At time 200 the particle is exactly on the node point being observed. The charge-conserving current weighting produces charges which agree with linear weighting of charge. Linear weighting to half cells produces a net charge which agrees with quadratic weighting of charge in one dimension, while the linear weighting to nodes followed by averaging to half cells does not correspond to any straightforward weighting of charge. Figure 15 shows the current weighted to a half-cell, which is used in Maxwell's curl equations to advance the fields. At time 150 the particle is located at the half cell being observed. The area under each curve, $\int Idt$, is identical for each weighting technique. Figure 15 may also be regarded as a diagram of the shape of a particle for current weighting purposes.

The disagreement between the charge given by the linear and charge-conserving weightings in Figure 14 is the error, and a source of the violation of Gauss's law in electromagnetic particle-in-cell simulations.

A.2 Two-dimensional non-conservation of charge

In two dimensions, the errors in charge that occur with the use of a non-charge-conserving current weighting are even more severe. Consider a bilinear current weighting to the half-nodes. A particle traveling obliquely to the mesh can leave behind a trail of permanent charges behind it due to flaws in the weighting. These residual charges sum to zero, but multipoles are left behind.

As an example, consider the charge on node A in Figure 16 due to a particle traveling uniformly along the line $\overline{abcde}$. The only weighted currents due to this particle which affect the charge at node A are I_{xA} and I_{yA}. The mesh is orthogonal and square, with $\Delta x = \Delta y$. The particle's velocity v_x in x and $v_x/2$ in y.

Only when the particle is traveling from point b to point c will any current weight to I_{xA}. (The x component of the current due to the particle is partially weighted to the half-node I_{xA}.) The net charge pushed into node A due to I_{xA} is:

$$q_1 = (\frac{qv_x}{\Delta x})(\frac{\Delta x}{2v_x})(\frac{1}{4})(\frac{1}{8}) \tag{42}$$

where $qv_x/\Delta x$ is the current , $\Delta x/2v_x$ is the time to traverse segment $\overline{bc}$, 1/4 is the weighting in the x direction to I_{xA}, and 1/8 is the weighting in the y direction.

Similarly, weighting to I_{yA} from segment $\overline{ce}$ yields a charge:

$$q_2 = -(\frac{qv_y}{\Delta y})(\frac{\Delta y}{2v_y})(\frac{1}{2})(\frac{1}{4}) \tag{43}$$

Even considering that $v_x = 2v_y$, there is a net charge left on node A of $-3q/64$.

Other nodes around the moving particle will exhibit similar errors, and another particle following in the same track will double all the errors, leading to charge accumulation which could severely affect the simulation.

References

[1] C.K. Birdsall and A. B. Langdon, *Plasma Physics Via Computer Simulation*,Adam Hilger (1991), pp. 360.

[2] R.W. Hockney and J.W. Eastwood *Computer Simulation Using Particles*, IOP Publishing (1988).

[3] A.B. Langdon, "On enforcing Gauss's law in electromagnetic particle-in-cell codes," Computer Physics Communications, July 1992, vol.70 (no.3): 447-50.

[4] B. Marder, "A method for incorporating Gauss's law into electromagnetic PIC codes," Journal of Computational Physics, Jan. 1987, vol.68 (no.1): 48-55.

[5] J. Villasenor and O. Buneman, "Rigorous charge conservation for local electromagnetic field solvers," Computer Physics Communications 69 (1992) 306-316.

[6] J.P. Verboncoeur, A.B. Langdon, and N.T. Gladd, "An object-oriented electromagnetic PIC code." Computer Physics Communications 87 (1995) 199-211.

[7] K.S. Yee, "Numerical solution of initial boundary-value problems involving Maxwell's equations in isotropic media," IEEE Trans. Ant. Prop., vol. AP-14, May 1966, pp. 302-307.

[8] Hewett, D.W.; Larson, D.J.; Doss, S., "Solution of simultaneous partial differential equations using Dynamic ADI: solution of the streamlined Darwin field equations," Journal of Computational Physics, July 1992, vol.101, (no.1):11-24.

[9] Nielsen, D.E., Drobot, A. T., "An analysis and optimization of the pseudo-current method," J. Comput. Phys. 89 (1990) 31.

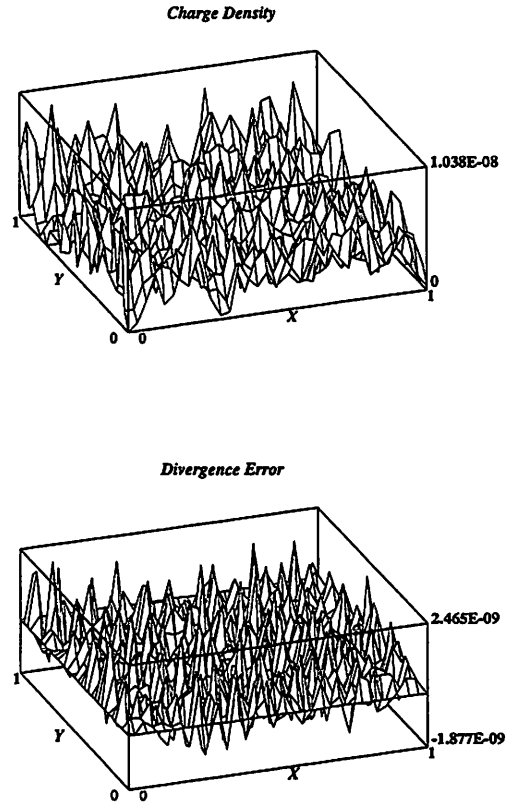

Figure 4: Charge density and divergence error (in C/m^3) in a relativistic beam simulation, with no corrections applied. Note that the magnitude of the error is about $1/4$ of the magnitude of the charge density, i.e., $\delta\rho/\rho \simeq 1/4$. Both graphs are noisy because of the small number of particles used.

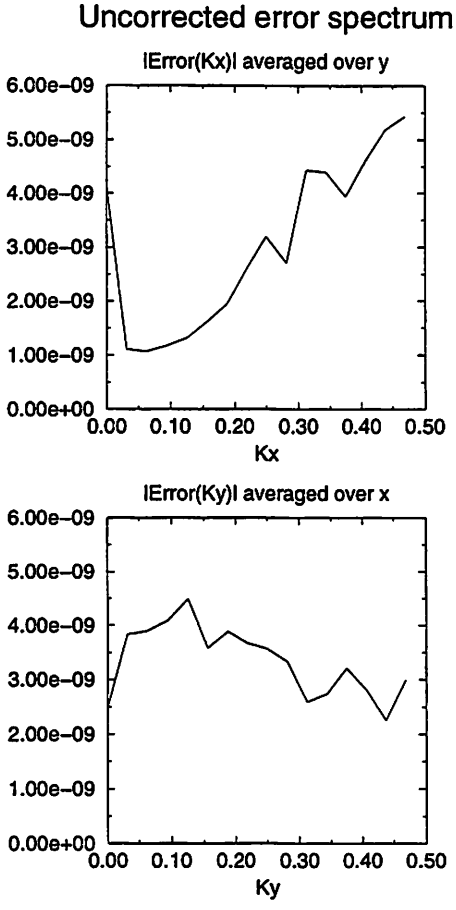

Figure 5: Error spectra in a simulation with no corrections applied. Note that not all the error is in short wavelengths. To obtain better statistics, the error was averaged in the direction opposite the FFT.

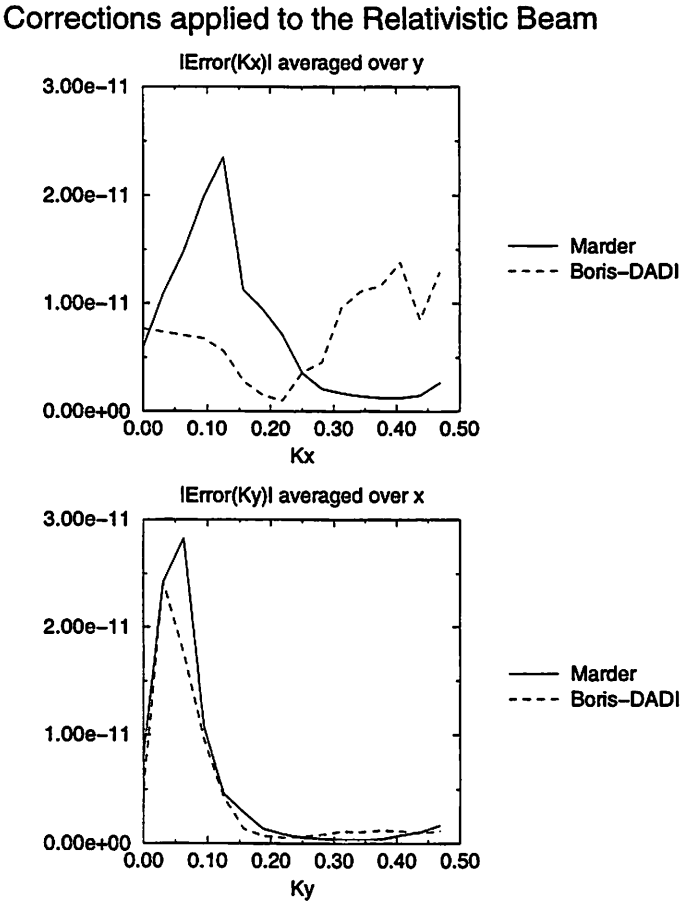

Figure 6: Error spectra after corrections are applied. 10 Langdon-Marder iterations were used, with $d = 0.8d_{max}$, while 2 DADI iterations were used. The error was reduced by a factor of more than 100.

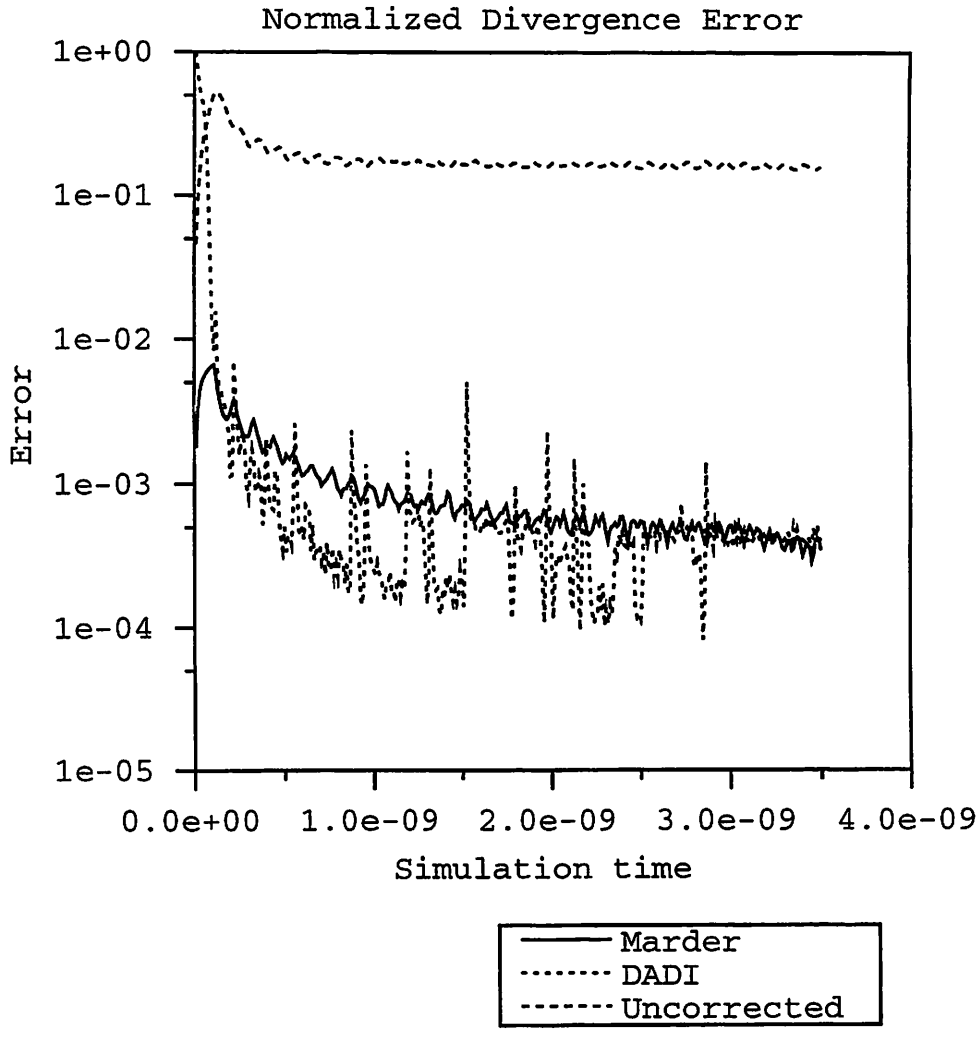

Figure 7: Normalized total error in the simulation.

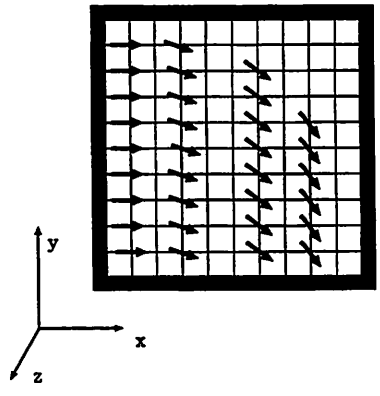

Figure 8: A beam curving in a magnetic field. Not shown is the leftward moving beam entering from the right hand side and curving upward. Such a beam is actually present in the simulation.

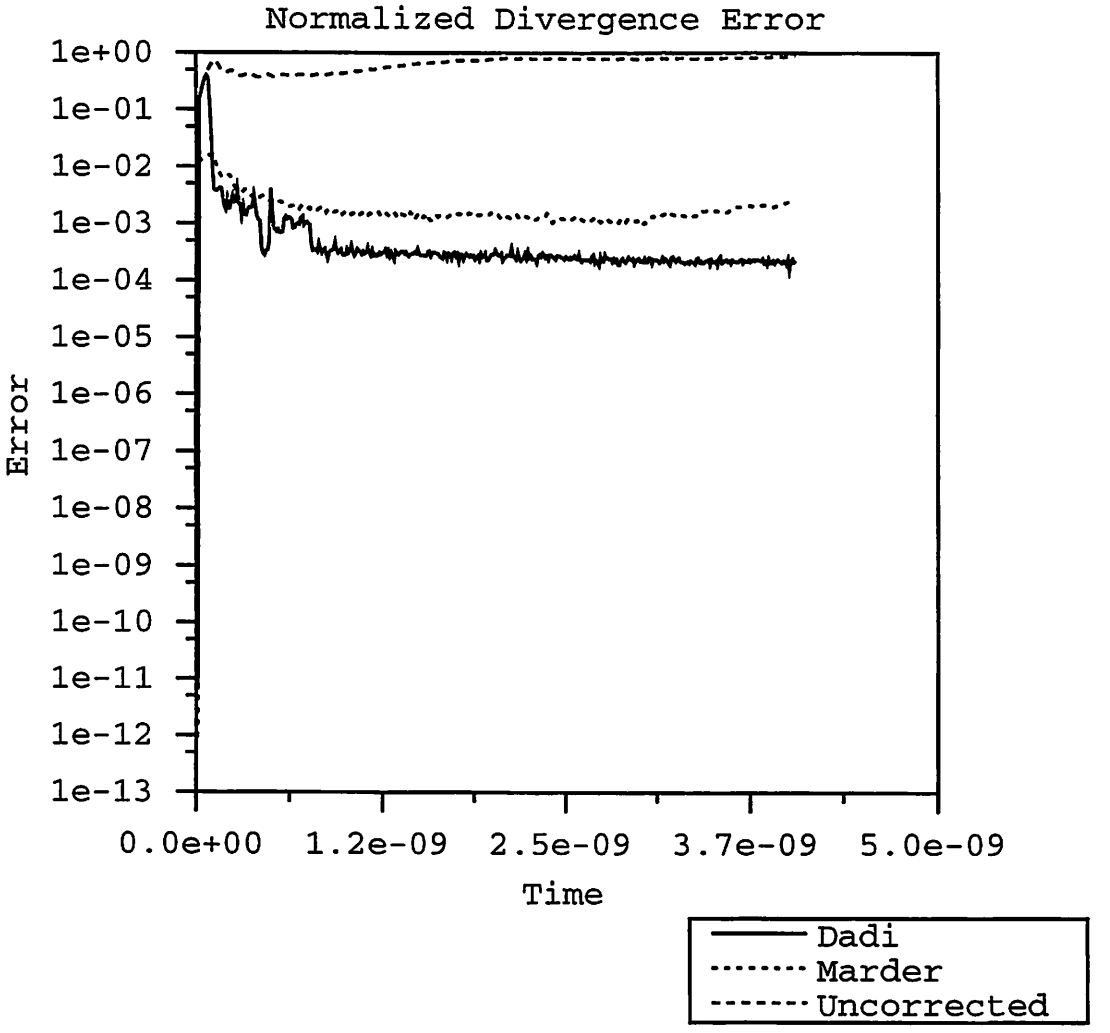

Figure 9: Errors for the curving beam.

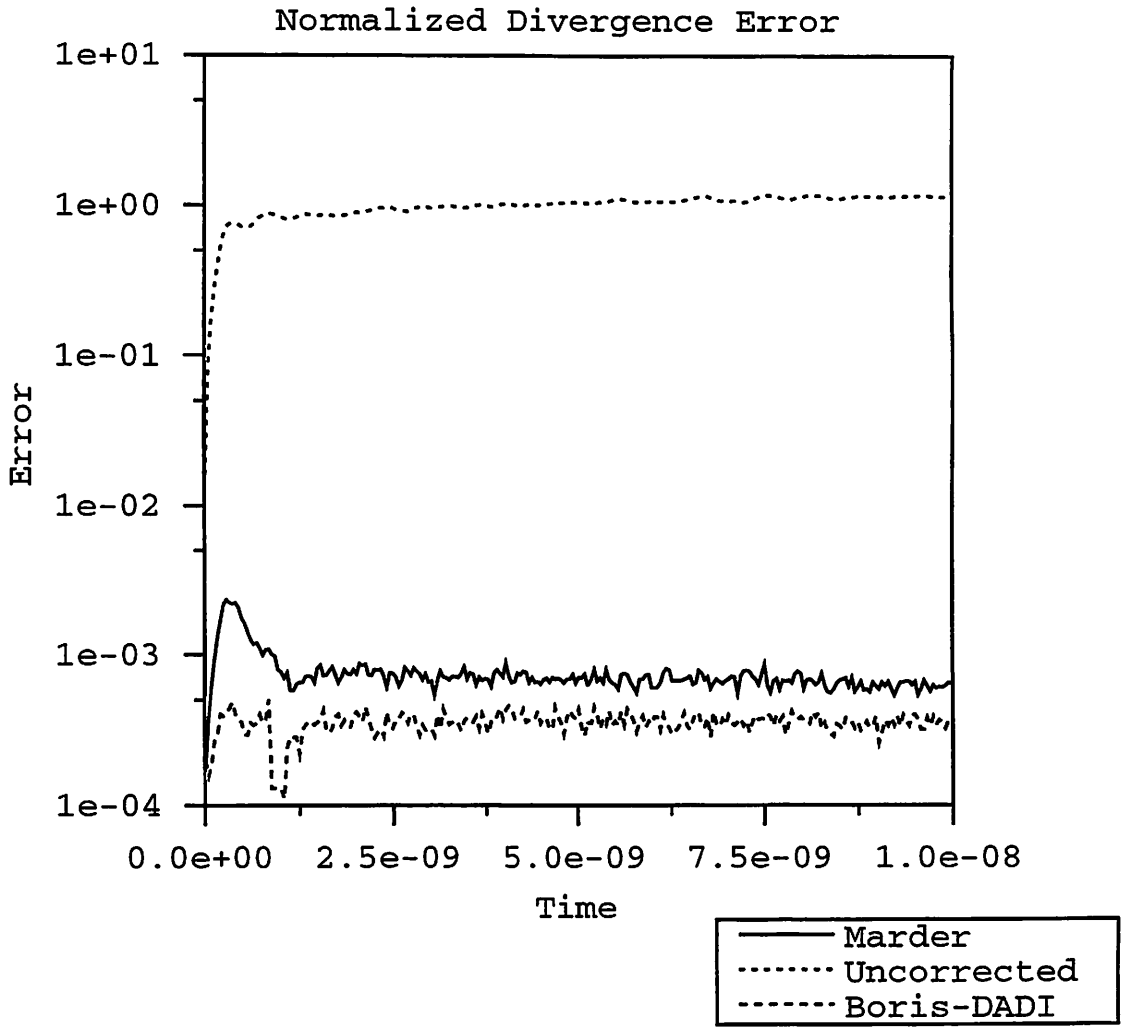

Figure 10: Errors for the thermal plasma.

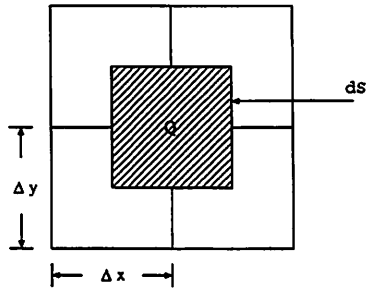

Figure 11: Typical Cell

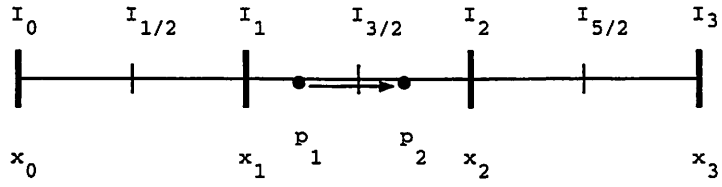

Figure 12: 1D example mesh. Here, x_j is the grid position, I_j is the current, and p_j is the particle position.

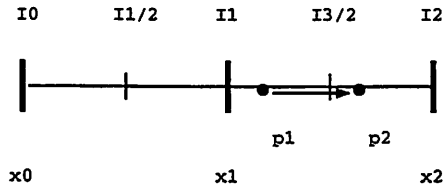

Figure 13: Current weighting to half-cells

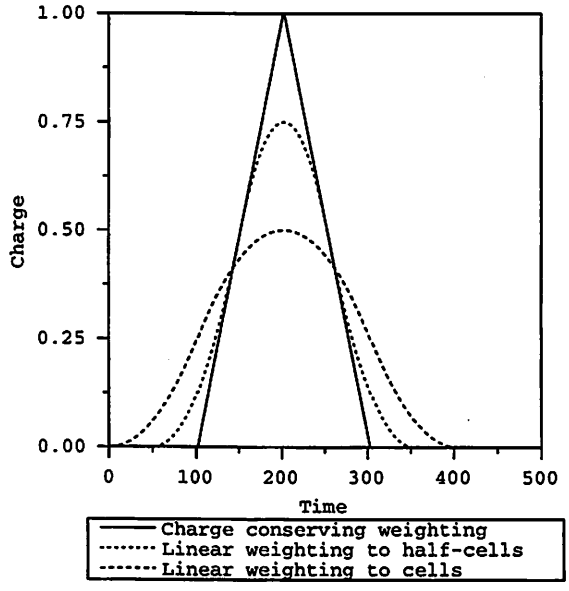

Figure 14: Net charge at a mesh point due to weighted current from a particle passing at a uniform velocity. The particle is on the mesh point at time 200. The two linear weightings distribute charge differently than the charge-conserving weighting, leading to error. See the text for details.

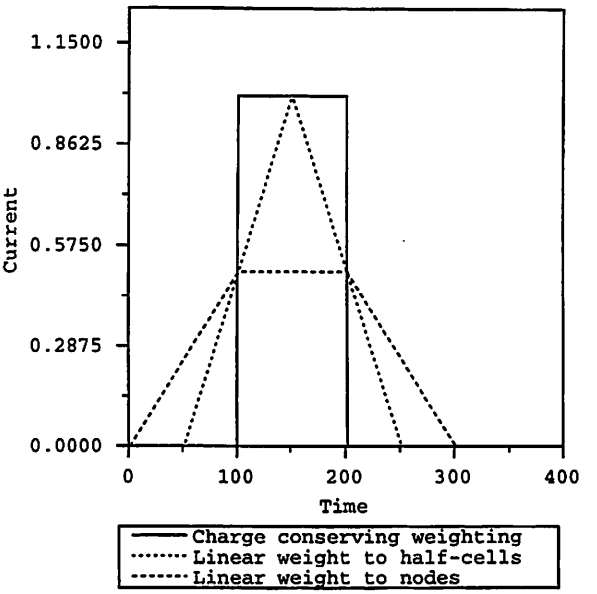

Figure 15: Current at a half-cell due to a particle passing at a uniform velocity. At time 150 the particle is located at the half cell being observed.

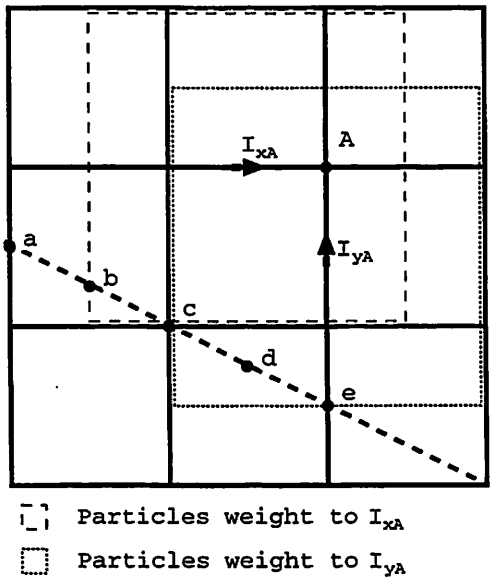

Figure 16: A particle traveling along **abcde** will leave a permanent charge at node A if a bilinear current weighting to half-cells is used.